Vision-Based Validation of a Strain-Based Rod Model Under Planar Bending

Annika Delucchi, Vincenzo Di Paola, Andreas Müller, and Matteo Zoppi

Abstract Manipulating continuum rods poses significant challenges as real-time shape reconstruction requires both high accuracy and low computational cost. While exact models generally do not satisfy real-time requirements, approximate models speed-up computation at the expense of accuracy. This work aims evaluates the performance of a strain-based cubic interpolation model in reconstructing the shape of a clamped-clamped rod for different tip poses. In particular, planar experiments are conducted to test the model's accuracy. As experimental studies in this context remain limited, this work aims to take a step toward real-world assessment. The results show excellent performance with a small relative error, between interpolated and exact models, of 0.84% when extracting the rod shape with a camera.

1 Introduction

Continuum rods are gaining increasing interest in the robotics community, serving as fundamental components in Tendon-Driven and Parallel Contin-

A. Delucchi
Department of Mechanical Engineering (DIME), University of Genoa, Italy
e-mail: annika.delucchi@edu.unige.it

V. Di Paola
Department of Mechanical Engineering (DIME), University of Genoa, Italy
e-mail: vincenzo.dipaola@edu.unige.it

A. Müller
Johannes Kepler University Linz, Linz, Austria
e-mail: a.mueller@jku.at

M. Zoppi
Department of Mechanical Engineering (DIME), University of Genoa, Italy
e-mail: matteo.zoppi@unige.it

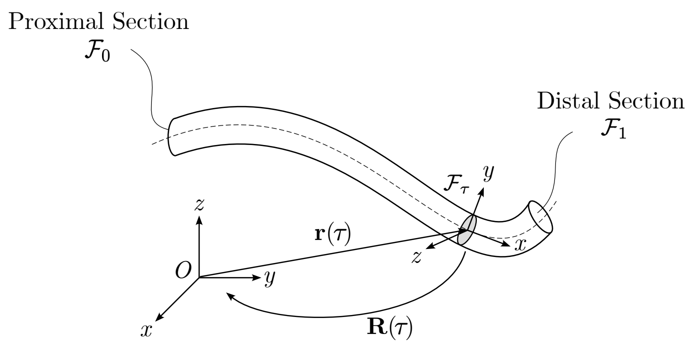

Fig. 1 Graphic representation of the main quantities involved in the geometric description of the rod. $\mathcal{F}_\tau$ is the material frame at τ, while $\mathcal{F}_0$ and $\mathcal{F}_1$ are the frames at the extremities of the rod. $\mathbf{R}(\tau)$ and $\mathbf{r}(\tau)$ are, respectively, the frame's orientation and position.

uum Robots or as end-effectors for dual manipulation tasks. Despite their versatility in applications ranging from surgical [**?**] to space orbital tasks [**?**], their elastic behaviour still poses crucial modelling challenges. Exact models consist in partial differential equations that are computationally expensive and often do not admit analytical solution. To overcome this mathematical complexity, researchers spent their effort into two main directions. The first one uses learning-based approaches, bypassing analytical complexity by training models on embedded features or vision data, to control the rod shape [**?**]. While real-time suitable, these often lack of generality compared to physics-based models. The second direction relies on approximate analytical models, leveraging beam theories to face the challenge posed by computational complexity and solution accuracy. Among the two, this work embraces the second one and studies the performance of a strain-based model [**?**] in reconstructing the shape of a clamped-clamped rod. Experiments assessing performance in this field are still limited and certainly not numerous. Therefore, this paper tries to move a step towards real world. In particular, rod models and their notation are briefly reviewed in Section 2. Experimental procedure, materials and methods are presented in Section 3. The Conclusion 4 wraps-up the results and future developments.

2 Rod Model

When speaking about rod models, probably, the foundational work carried out by [**?**] is a major reference in the field. In their work, the concept of Finite Element Method (*FEM*) is extended considering rotations in addition to displacements, leading to the well-known Geometrically Exact *FEM* (*GE-FEM*). Under the small-deformation assumption, subsequent developments shifted the approximation from *displacements* to *strain fields*, first considering piecewise-constant strains [**?**] and later variable strain formulations [**?**], [**?**], [**?**]. This section recalls the main equations of the variable curvature strain-based model presented in [**?**]. In particular, the extensive use of Lie group properties is made to both get insight on rod physics and fasten the computation [**?**], [**?**]. Let us consider a slender rod whose elastic behaviour can be described with an inextensible Kirchhoff model. Call with $\tau \in [0,1]$ the normalised material coordinate and express with $\mathbf{R}(\tau)$ and $\mathbf{r}(\tau)$ the orientation and the position of the material frame at τ. The $x-$axis of the frame will be aligned with the rod centreline, as shown in Figure 1. The frame's spatial evolution can be described as a function of the canonical coordinates $\mathbf{x}$ yielding the curvature as $\boldsymbol{\kappa}(\tau) = \mathbf{dexp}_{\mathbf{x}(\tau)}\mathbf{x}'(\tau)$ and the position derivative as $\mathbf{r}'(\tau) = \exp\, \tilde{\mathbf{x}}(\tau)\,\mathbf{e}_1$, with $(\cdot)' = \partial/\partial\tau$. Imposing twists and their derivatives using a cubic interpolation yields a polynomial approximating the canonical coordinate $\mathbf{x}^{[3]}$ and, consequently, the curvature $\boldsymbol{\kappa}^{[3]}$ and the position $\mathbf{r}^{[3]}$. Therefore, a third-order approximation of the solution of the above *ODE* for $\mathbf{x}(\tau)$ is

$$\mathbf{x}^{[3]}(\tau) = (3\tau^2 - 2\tau^3)\mathbf{x}_1 + \tau(\tau-1)^2\boldsymbol{\kappa}_0 + (\tau^3 - \tau^2)\mathbf{dexp}^{-1}_{-\mathbf{x}_1}\boldsymbol{\kappa}_1,$$

with $\boldsymbol{\kappa}_0$, $\boldsymbol{\kappa}_1$ initial and final curvature values, $\mathbf{x}_1$ final twist and $\mathbf{dexp} : so(3) \to so(3)$ differential of the exponential map [**?**]. The derivative of $\mathbf{x}^{[3]}$ yields the curvature

$$\boldsymbol{\kappa}^{[3]}(\tau) = \mathbf{dexp}_{\mathbf{x}^{[3]}(\tau)}\mathbf{x}'^{[3]}(\tau). \tag{1}$$

The position is also obtained in terms of $\mathbf{x}^{[3]}(\tau)$ and can be integrated by quadrature

$$\mathbf{r}^{[3]}(\tau) = \frac{\tau}{2}\Big(\sum_{i=1}^{s} \alpha_i \exp\mathbf{x}^{[3]}\,\bar{p}_i\,\mathbf{e}_1\Big), \tag{2}$$

with $\mathbf{e}_1 = \begin{pmatrix}1 & 0 & 0\end{pmatrix}^{\mathrm{T}}$ unit vector, α_i Legendre weights and $\bar{p}_i := \frac{1}{2}(1+p_i)\tau$ and p_i Gauss points. At this point, the shape reconstruction problem, where the rod tips are imposed, can be reformulated as a Boundary Value Problem (*BVP*). While typically one is taken as the identity $\mathbf{R}_0 = \mathbf{I}$, $\mathbf{r}_0 = \begin{pmatrix}0 & 0 & 0\end{pmatrix}^{\mathrm{T}}$, the other is prescribed in terms of $\mathbf{x}_1$ and $\mathbf{r}_1$. The interpolation structure, that is substituing Eq. (1) into Eq. (2), implicitly satisfies orientation requirements when position ones are met, yielding a sole geometric constraint to satisfy. Therefore, the *BVP* is recast into a constrained energy minimization problem subject to the sole tip position constraint

$$\begin{aligned} &\min_{\boldsymbol{\kappa}_0,\boldsymbol{\kappa}_1} V^{[3]}_{\boldsymbol{\kappa}}(\mathbf{x}_1,\boldsymbol{\kappa}_0,\boldsymbol{\kappa}_1) \\ \text{s.t.}\quad &\mathbf{g}(\boldsymbol{\kappa}_0,\boldsymbol{\kappa}_1) = \mathbf{r}_1 - \mathbf{r}(1) = \mathbf{0}, \end{aligned} \tag{3}$$

with potential energy obtained by quadrature

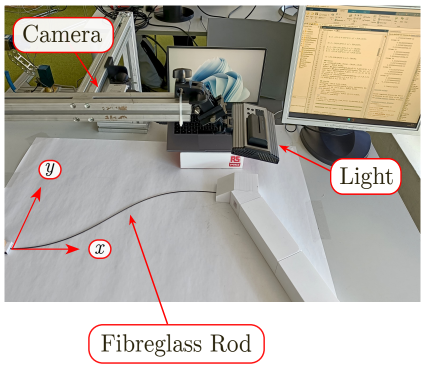

Fig. 2 Experimental setup.

Fibreglass Rod Parameters	
Young's Modulus	35×10^9 Pa
Shear Modulus	3×10^9 Pa
Diameter	2×10^{-3} m
Length	0.6 m
Camera Parameters	
Focal length x	604.51 px
Focal length y	606.07 px
Principal point x	655.22 px
Principal point y	362.41 px
Camera height	0.324 m

Table 1 System parameters.

$$V_{\boldsymbol{\kappa}}^{[3]}(\mathbf{x}_1, \boldsymbol{\kappa}_0, \boldsymbol{\kappa}_1) = \frac{1}{2} \sum_{i=1}^{s} \alpha_i (\boldsymbol{\kappa}^{[3]}(\tau) - \bar{\boldsymbol{\kappa}}^{[3]}(\tau))^{\mathrm{T}} \mathbf{K}_{\boldsymbol{\kappa}} (\boldsymbol{\kappa}^{[3]}(\tau) - \bar{\boldsymbol{\kappa}}^{[3]}(\tau)), \quad (4)$$

where $\mathbf{K}_{\boldsymbol{\kappa}}$ is the bending-torsion stiffness matrix, $\bar{\boldsymbol{\kappa}}$ is the reference curvature and $\mathbf{R} = \exp \mathbf{x}_1$ is the prescribed tip orientation, with $\exp : so(3) \to SO(3)$. The minimization problem fully describes the kineto-static problem [**?**]. Notice that it can be solved with a Newton-Raphson iterative scheme which updates the initial and final curvature parameters $\boldsymbol{\kappa}_0$ and $\boldsymbol{\kappa}_1$ until convergence is met. This formulation potentially admits analytical closed form, lowering the computational cost.

3 Experiments

The aim of the experiments consists in assessing the model's accuracy when reconstructing the shape of a fibreglass rod clamped at both ends. Indeed, the metric used here consists in comparing the interpolated model solution with the experimental measure of the rod shape; the same is done with the numerical exact model. The experimental shape is retrieved via images acquired using a camera and exploiting the contrast between the rod and the background to extract the rod profile [**?**]. Other common strategies involve force measurements [**?**] or recognition of features embedded on the rod, such as ArUco markers [**?**] or virtual features [**?**].

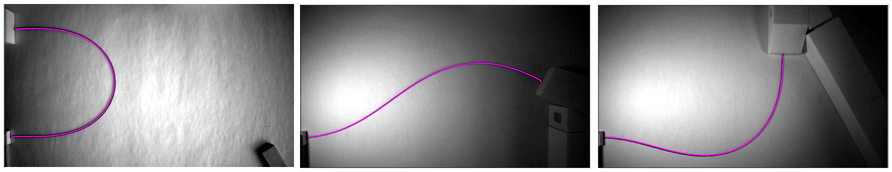

Fig. 2 Reconstructed rod shape in pixels (magenta) overlaid on the original image.

3.1 Set-up and Assumptions

The procedure uses a planar setup with the rod lying entirely on a plane assumed parallel to the camera's image plane. This geometric assumption allows using a single camera for shape extraction. Moreover, the influence of gravity can be neglected reducing the sources of error while measuring. The rod parameters can be found in Table 1. In this case, since the rod is slender, assuming the material isotropic is acceptable and realistic. The hardware used for the mentioned tests is shown in Figure 2. It consists of a support frame holding a camera[1] and two bar lights, oriented down looking at the table. The camera parameters are reported in Table 1, while its alignment is set with a digital inclinometer ensuring planarity and minimizing perspective distortions. Images are then collected through a laptop and processed with MATLAB. The area of interest is covered in white while the rod is painted with black to maximize contrast reducing the sources of error. Meanwhile, the rod tips are clamped using ad-hoc plastic blocks designed to automatically set the desired angles with respect to the fixed reference.

3.2 Shape Extraction Procedure

The rod shape is reconstructed using a skeletonization process, reducing the rod profile, *i.e.* centreline, to single-pixel-wide curves. In particular, skeletonization produces multiple possible skeleton branches, among which the rod centreline is selected. The selection can be made in several ways, here the longest branch is used while discarding short spurs due to reflections or background objects. Figure 2 shows an example of reconstructed skeleton pixels overlaid in magenta on the original image. The pixels are then transformed into ordered coordinates and interpolated to obtain a continuous representation of the rod. Two sorting strategies were investigated. A nearest-neighbour method, that orders points by greedily selecting the closest unvisited neighbour, starting from the leftmost pixel. While computationally efficient, this approach is noise sensitive and tends to preserve local pixel-level

[1] Intel Real Sense D405 with RGB resolution of 1280×720, frame rate of 30 fps and an operative range of $0.07 - 0.50$ m.

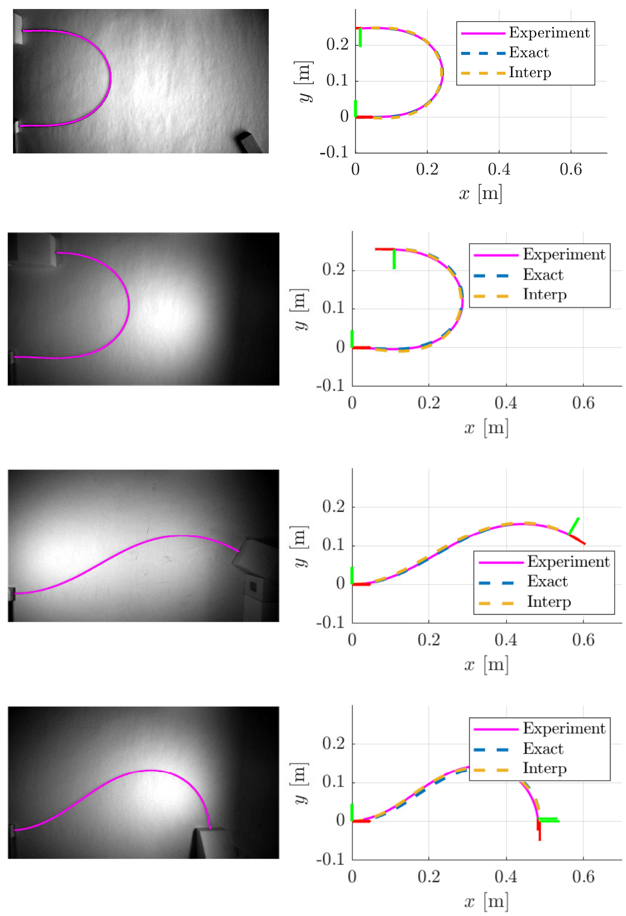

Fig. 3 Experimental shape extraction. Left: original image with the centreline's pixels. Right: comparison between experimental, interpolated and exact shapes.

irregularities, resulting in oscillatory reconstructions. On the other hand, a graph-based strategy computes the shortest path between the two farthest endpoints of the skeleton, yielding a geodesic curve that captures the rod shape using only 30%–50% of the skeleton points. Although computationally demanding, it provides greater robustness and smoothness. In this work, only results obtained with the graph-based algorithm are presented. However, for a discussion on the nearest-neighbour algorithm the reader is referred to [**?**].

	MEAN [m]		STD DEV [m]		MAX [m]	
Exact	4.2×10^{-3}	0.70%	2.2×10^{-3}	0.37%	1.75×10^{-2}	2.9%
Interp	4.7×10^{-3}	0.78%	2.4×10^{-3}	0.40%	1.75×10^{-2}	2.9%

Table 2 Standard deviation, mean and maximum errors of exact and interpolated models against experimental reference.

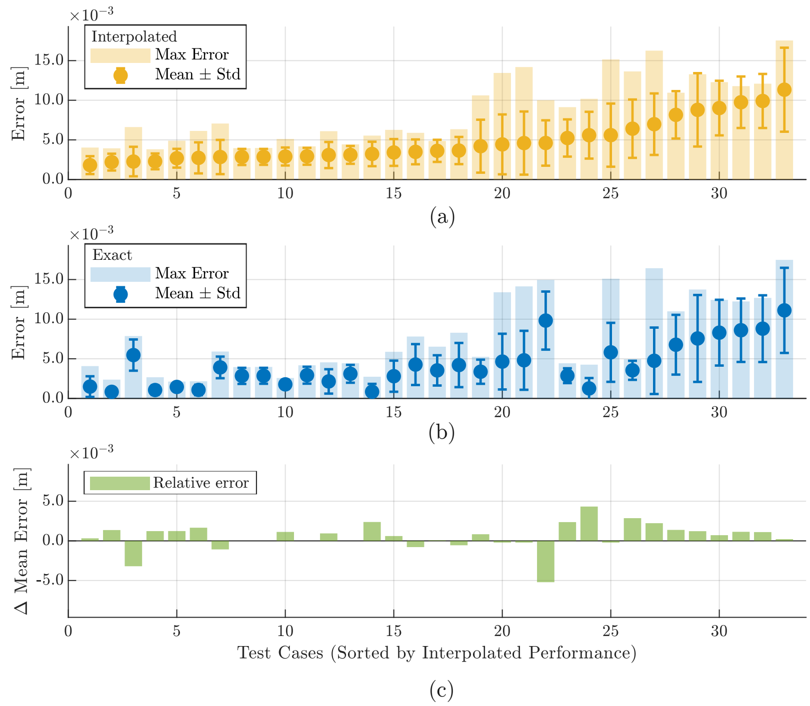

Fig. 4 For each test case, the mean, standard deviation and maximum errors are reported for (a) the interpolated model and (b) the exact model, while (c) reports the relative errors.

3.3 Results

A total of 33 non-overlapping rod shapes are analysed, ranging from U- and S-shapes to chart-like shapes, see Figure 2. For each test, a single frame is used to extract the centreline and compare it against the models. Three shapes are depicted in Figure 3 where, on the left, the results of the extraction are reported while, on the right, simulations and experiments meet. Thus, the quantitative analysis is based on point-wise shape error, defined as

$$e(\tau) = ||\mathbf{r}_{\text{model}}(\tau) - \mathbf{r}_{\text{exp}}(\tau)||. \tag{5}$$

Figure 4 and Table 2 summarise the results across all tests. For each of them, the mean configuration error, its standard deviation and the maximum error are reported. Since the tests are independent and their order is not informative, results are sorted by increasing the mean error of the interpolated model Figure 4-(a), with the corresponding exact model results Figure 4-(b) following the same ordering. Moreover, for each test, the difference between the exact and interpolated mean errors Figure 4-(c) is also reported, here referred as relative error. The mean shape error for the interpolated model remains below 0.78% of the rod length (4.7×10^{-3} m), while the maximum error does not exceed 2.9%. The tests with higher errors are common to both models, suggesting that these discrepancies are primarily due to uncertainty in shape extraction rather than modelling errors alone. The exact model achieves slightly lower mean 0.70% and maximum 2.9% errors, although the improvement is marginal. The relative discrepancy between the exact and interpolated solutions remains below 0.84%, 5.2×10^{-3} m in test 22, when the interpolated model performs better than the exact and below 0.71%, 4.3×10^{-3} m in test 24, when the exact model result is more accurate than the interpolated.

4 Conclusion

This work proposes a strategy to evaluate the performance of strain-based rod models. Vision-based experiments were conducted in a planar setting, extracting the rod shape with a skeletonization approach. Then, the accuracy of an existing strain-based interpolation model was evaluated comparing its predictions with experimental shapes and numerically exact solutions. Across all the tests, the maximum deviation from the experimental shape remained below 2.9% of the rod length, with an average error of 0.78%. These results indicate that the interpolation approach provides a reliable rod approximation within the considered operating regime, while also highlighting the role of experimental uncertainty in the observed discrepancies. For tightly bent shapes, the fibreglass rod can experience instabilities, slipping out of the working plane. While these cases were excluded from this planar analysis, they highlight the need for spatial methods. However, generalizing the skeletonization approach would require additional cameras and frame synchronization, which could be complex. Consequently, a different shape extraction method has been adopted for spatial validation [**?**].

Acknowledgements The third author acknowledges support by the LCM-K2 Center within the Austrian COMET-K2 program, and by the Austrian Science Fund (FWF) [I4452-N]

References

1. Almaghout, K., Cherubini, A., Klimchik, A.: Robotic Co-Manipulation of Deformable Linear Objects for Large Deformation Tasks. Elsevier (2024). DOI 10.1016/j.robot.2024.104652
2. Boyer, F., Lebastard, V., Candelier, F., Renda, F.: Dynamics of Continuum and Soft Robots: A Strain Parameterization Based Approach. IEEE Transactions on Robotics (2021). DOI 10.1109/tro.2020.3036618
3. Burgner-Kahrs, J., Rucker, D.C., Choset, H.: Continuum Robots for Medical Applications: A Survey. IEEE Transactions on Robotics (2015). DOI 10.1109/tro.2015.2489500
4. Caro, S., Chevallereau, C., Remus, A.: Manipulating Deformable Objects with a Dual-Arm Robot. ROBOVIS 2021: 2nd International Conference on Robotics, Computer Vision and Intelligent Systems (2021). DOI 10.5220/0010707600003061
5. Delucchi, A.: Dual-Arm Robotic Manipulation of Continuum Rods. Master's thesis, University of Genova (2025)
6. Delucchi, A., Di Paola, V., Müller, A., Zoppi, M.: Performance and experimental analysis of strain-based models for continuum robots (2026)
7. Češarek, P., Saje, M., Zupan, D.: Dynamics of Flexible Beams: Finite-Element Formulation Based on Interpolation of Strain Measures. Finite Elements in Analysis and Design (2013). DOI 10.1016/j.finel.2013.04.001
8. Müller, A.: Review of the Exponential and Cayley Map on SE(3) as Relevant for Lie Group Integration of the Generalized Poisson Equation and Flexible Multibody Systems. Proceedings of the Royal Society A: Mathematical, Physical and Engineering Sciences (2021). DOI 10.1098/rspa.2021.0303
9. Müller, A.: Fourth-Order Accurate Strain-Parameterized Shape Representation of Beam Elements for Modeling Continuum Robots and Robotic Manipulation of Slender Objects. Journal of Mechanisms and Robotics (2024). DOI 10.1115/1.4066904
10. Renda, F., Boyer, F., Dias, J., Seneviratne, L.: Discrete Cosserat Approach for Multisection Soft Manipulator Dynamics. IEEE Transactions on Robotics (2018). DOI 10.1109/tro.2018.2868815
11. Selig, J.M.: Geometric Fundamentals of Robotics. Springer (2004)
12. Simo, J.: A Finite Strain Beam Formulation. The Three-Dimensional Dynamic Problem. Part I. Computer Methods in Applied Mechanics and Engineering (1985). DOI 10.1016/0045-7825(85)90050-7
13. Takano, R., Mochiyama, H., Takesue, N.: Real-Time Shape Estimation of Kirchhoff Elastic Rod Based on Force/Torque Sensor. In: 2017 IEEE International Conference on Robotics and Automation (ICRA). IEEE (2017). DOI 10.1109/icra.2017.7989292
14. Ticozzi, L., Vela, P.A., Tsiotras, P.: Modeling and Control of a Hybrid Soft–Rigid Space Manipulator System. Journal of Guidance, Control and Dynamics (2025). DOI 10.2514/1.g009231
15. Till, J., Rucker, D.C.: Elastic Stability of Cosserat Rods and Parallel Continuum Robots. IEEE Transactions on Robotics (2017). DOI 10.1109/tro.2017.2664879
16. Yu, M., Lv, K., Zhong, H., Song, S., Li, X.: Global Model Learning for Large Deformation Control of Elastic Deformable Linear Objects: An Efficient and Adaptive Approach. IEEE Transactions on Robotics (2023). DOI 10.1109/tro.2022.3200546